Journal of Materials Chemistry C

ROYAL SOCIETY OF CHEMISTRY

PAPER

View Article Online
View Journal | View Issue

Cite this: J. Mater. Chem. C, 2024, 12, 11955

Negative thermal expansion in $Sc_2Mo_3O_{12}:Sm^{3+}$ for white LEDs and unveiling the impact of phase transition on cryogenic luminescence†

Annu Balhara,[ab] Santosh K. Gupta,[ab]* Malini Abraham,[cd] Ashok Kumar Yadav,[e] Mohsin Jafar[f] and Subrata Das[cd]

Received 3rd May 2024,
Accepted 25th June 2024

DOI: 10.1039/d4tc01817f

rsc.li/materials-c

Red-emitting phosphors are essential to achieve sustainable white-light-emitting diodes (WLEDs) for lighting and indoor plant growth. Materials with negative thermal expansion (NTE) can overcome the critical problem of the thermal quenching (TQ) of photoluminescence (PL). In this regard, we report a $Sc_2Mo_3O_{12}:Sm^{3+}$ (SMO:Sm^{3+}) reddish-orange emitting phosphor with no TQ up to 433 K. The intense charge transfer from the SMO matrix to the dopant ($O^{2-} \rightarrow Sm^{3+}$) reinforced the absorption of ultraviolet (UV) light, in addition to intra 4f–4f blue light excitation. The site occupation of Sm^{3+} was investigated using extended X-ray absorption fine structure (EXAFS) spectroscopy, and X-ray absorption near edge structure (XANES) spectroscopy ruled out any contribution of Sm^{2+} in the PL process. Temperature-dependent XRD studies revealed strong NTE in SMO, which induced promising anti-TQ performance *via* intensifying the charge transfer absorption and improved structural rigidity. As a result, 591% of its intensity at room temperature was retained at 433 K resulting in a ~6-fold enhancement in Sm^{3+} emission. Moreover, we demonstrated two prototypes for lighting and indoor plant growth by fabricating the SMO:Sm^{3+} phosphor onto UV (280 nm) and 410 nm LED chips, respectively. The WLED offers a high color rendering index (CRI) of 84, CIE (0.33, 0.32), and correlated color temperature (CCT) of 5408 K, with a high luminous efficacy of 113 lm W^{-1}. The LED emission bands overlap with the absorption of phytochrome, P_R, which is essential for plant growth. We further investigated the temperature-dependent cryogenic PL properties and its correlation with phase transition. These findings revealed that the lattice phase transition has minimal impact on the Sm^{3+} local structure and its luminescence profile. Interestingly, we discovered the green emission of the monoclinic SMO phase at liquid nitrogen temperature (−193 °C). The MoO_4^{2-} emission diminished on phase transition from monoclinic to orthorhombic SMO at room temperature. Our results demonstrate the potential of SMO:Sm^{3+} phosphors for applications in lighting and indoor plant growth LEDs with anti-TQ properties.

1. Introduction

The thermal quenching (TQ) of the photoluminescence (PL) of rare earth (RE^{3+})-activated phosphors at elevated temperatures has been a serious concern for the development of efficient phosphor-converted white light emitting diodes (pc-WLEDs).[1–7] Consequently, the non-radiative losses due to the positive thermal expansion behaviour of the majority of the host matrices have led to lower PL efficiency. Phosphor materials are a key component of WLEDs, and thermal stability is determined on the basis of different parameters such as crystal structure, thermal expansion coefficients, chemical composition, and structural rigidity.[1] The main challenge is to overcome the PL intensity loss for phosphors used in high-power LED chips, where the heat generation can result in an increase in the temperature of the chip surface up to 150 °C or higher.[1] The phonon vibrations are activated at elevated temperatures, which induces non-radiative processes that are detrimental for the PL intensity. Hence, phosphor materials with excellent thermal stability have been investigated for the design of practical WLEDs in recent years.[8–11] Some of the promising approaches for improving the LED performance at elevated

[a] Radiochemistry Division, Bhabha Atomic Research Centre, Trombay, Mumbai-400085, India. E-mail: santoshg@barc.gov.in, santufrnd@gmail.com
[b] Homi Bhabha National Institute, Mumbai 400094, India
[c] Materials Science and Technology Division, CSIR-National Institute for Interdisciplinary Science and Technology, Thiruvananthapuram, Kerala 695019, India
[d] Academy of Scientific and Innovative Research (AcSIR), Ghaziabad 201002, India
[e] Atomic & Molecular Physics Division, Bhabha Atomic Research Centre, Mumbai 400085, India
[f] Chemistry Division, Bhabha Atomic Research Centre, Trombay, Mumbai 400085, India

† Electronic supplementary information (ESI) available. See DOI: https://doi.org/10.1039/d4tc01817f

temperatures have been explored, such as defect engineering, negative/zero thermal expansion, control of dopant lattice sites, improving crystallinity, enhanced structural rigidity, and energy transfer.[3,6,12,13]

In past years, host materials with negative thermal expansion (NTE) property have attracted considerable research interests, and such materials have been well explored in the realm of opto-electronics and high-temperature devices applications.[14–16] Since the report on the first NTE material, ZrW_2O_8 in 1996,[17] different RE^{3+}-doped NTE materials have been investigated for solid-state lighting applications. In recent years, several host materials of the $A_2M_3O_{12}$ family (where A is a trivalent metal, *i.e.*, lanthanide ion (Ln^{3+}) or transition metal (TM^{3+}), and M = W, Mo) presented good chemical flexibility and a wide-ranging NTE effect.[16,18] $Sc_2Mo_3O_{12}$ is one of the promising NTE materials of this family. It offers advantages, such as low temperature synthesis, strong NTE, and excellent chemical stability.[18–21] $Sc_2Mo_3O_{12}$ exists in the orthorhombic and monoclinic phases, and undergoes a temperature-responsive phase transition between the two phases. The orthorhombic phase displays a strong NTE and is stabilized in the temperature range of −93 °C to 800 °C, with a high average thermal expansion coefficient (-6.3×10^{-6} °C^{-1}).[5,16,22] Recently, Liao *et al.*[5] reported on a two-dimensional NTE in a $Sc_2Mo_3O_{12}$:Yb/Er phosphor, which led to a 45-fold enhancement in upconversion emissions. Mao and group reported on a $Sc_2Mo_3O_{12}$:Eu phosphor and discussed the energy transfer induced by NTE, which resulted in the anti-thermal quenching of Eu^{3+} luminescence.[3] Back in 2014, Wu *et al.*[18] investigated the thermal expansion and phase transition in $Sc_{2-x}Fe_xMo_3O_{12}$. Following this, Romao *et al.*[23] explored the thermal expansion in a series of isomorphic $A_2B_3O_{12}$ materials using computational methods.

One of the important aspects of the $Sc_2Mo_3O_{12}$ matrix is the reversible phase transition from the monoclinic to orthorhombic phase at a temperature of −93 °C (180 K) on heating and cooling cycles.[24,25] Young *et al.*[26] investigated the monoclinic → orthorhombic phase transition, and concluded that the formation of mix-orthorhombic–monoclinic phases occurs in the temperature range of 160 to 220 K. Thus, an investigation of the temperature-dependent structural phase transition and its impact on the PL properties of $Sc_2Mo_3O_{12}$ and Sm^{3+} ions will be interesting, and is crucial to understand the structure–property relationship.

The current pc-WLEDs mainly consist of the yellow $Y_3Al_5O_{12}$:Ce^{3+} (YAG:Ce) phosphor coated on a blue InGaN LED chip. The WLEDs are widely used for indoor lighting, but the commercialization of blue LED chip-based lighting devices has raised severe concerns of blue-light hazards in our daily life.[9] Additionally, the deficiency of the red spectrum results in a low color rendering index (CRI) with Ra < 80 and high correlated color temperature (CCT).[4,27] The approach of combining the LED chip with a rational mixture of blue, green, and red phosphors appeared to be promising for elucidating the blue light component from WLEDs and realization of sustainable lighting. Therefore, the exploration of novel red-emitting phosphors for WLEDs has aroused great scientific interests in recent years. In this context, several Eu^{3+}, Sm^{3+} and Mn^{4+}-doped phosphors have been investigated in order to develop sustainable WLEDs devices with efficient brightness, high CRI, optimum CCT and robust thermal stability.[4,7,14,28–31] Recently, Sm^{3+}-activated phosphors have been explored to develop WLEDs with high luminous efficiency and to fulfil the deficiency of the red component.[32–38] Grigorjevaite *et al.*[39] reported on the $K_2Bi(PO_4)(MoO_4)$:Sm^{3+} phosphors, and developed LEDs for horticultural and lighting applications. Li *et al.*[40] developed a thermally stable pc-WLED using the reddish-orange emitting $Ba_3LaNb_3O_{12}$:Sm^{3+} phosphor. However, the absorption efficiency of the Sm^{3+} phosphors for ultraviolet (UV) and near-UV light is low, and the 4f–4f intra-transitions of Sm^{3+} have a low absorption coefficient. Hence, the development of novel Sm^{3+}-activated phosphors that exhibit strong charge transfer (CT) from the host matrix to Sm^{3+} in the UV and near-UV region will contribute immensely in the development of efficient and sustainable WLEDs.

In this work, we developed a novel $Sc_2Mo_3O_{12}$:Sm^{3+} phosphor using low temperature solid-state synthesis. High temperature-dependent X-ray data were used to investigate the NTE property of the $Sc_2Mo_3O_{12}$:Sm^{3+} phosphor in the temperature range of 300 to 700 K. The oxidation state and site occupation of Sm ions in $Sc_2Mo_3O_{12}$ were confirmed by X-ray absorption spectroscopy, *viz.*, extended X-ray absorption fine structure (EXAFS) and X-ray absorption near edge structure (XANES) measurements. Temperature-dependent PL studies from room temperature to 433 K were carried out to study the effect of NTE on thermal quenching. The $Sc_2Mo_3O_{12}$:Sm^{3+} phosphor displayed NTE, which improved the structural rigidity and induced strong charge transfer (CT) between the MoO_4^{2-} and Sm^{3+} ions. This resulted in enhanced emission intensity at elevated temperature. Thus, the $Sc_2Mo_3O_{12}$:Sm^{3+} phosphor shows the anti-thermal quenching of the Sm^{3+} luminescence. Temperature-dependent PL studies at cryogenic temperatures (80 to 300 K) were performed to investigate the impact of the phase transition of $Sc_2Mo_3O_{12}$ on the luminescence properties of the Sm^{3+} ions. Finally, the designed red phosphor was explored to fabricate WLEDs with improved color rendering index and indoor plant growth. This study is an effort to study the relationship between the NTE, phase transition and anti-thermal quenching of luminescence, which will provide important insights into the development of sustainable WLEDs.

2. Experimental methods

2.1. Synthesis

A series of $Sc_{2-2x}Sm_{2x}Mo_3O_{12}$ (x = 0.01, 0.03, 0.05, 0.07, and 0.10 mol) samples were prepared by conventional solid state synthesis protocol in sealed condition to avoid the loss of the molybdenum trioxide reagent. The doping amount of Sm^{3+} was considered with respect to the initial Sc sites. Binary constituent oxides, *viz.*, Sc_2O_3 (Indian Rare Earths Ltd, purity 99.9%) and Sm_2O_3 (Indian Rare Earths Ltd, purity 99.9%), were heated for 12 h at 800 °C in order to get rid of the adsorbed moisture and oxy-carbonates. MoO_3 (Sigma Aldrich and purity 99.9%)

was heated for 2 h at 200 °C to get rid of the adsorbed moisture. Stoichiometric amounts of each of the binary reagents were then weighed carefully, and ground homogenously in an agate mortar and pestle for 2 h. Each of the nominal compositions was then pelletized, kept in a quartz crucible, evacuated and sealed to prevent the loss of molybdenum oxide. The sealed crucible was then given a heat treatment at 800 °C for 12 h. The crucibles were allowed to cool down, and the pellets were then broken and the obtained products were characterized by powder X-ray diffraction technique. For ease, the Sm-doped samples are referenced according to the mole% of Sm with respect to the Sc sites. For example, 1% Sm indicates that the sample composition is $Sc_{2-2x}Sm_{2x}Mo_3O_{12}$ with $x = 0.01$. The characterization details are provided in Section S1 of the ESI.†

3. Results and discussion

3.1. Structural and morphological analysis

The XRD patterns of the $Sc_2Mo_3O_{12}$:xSm^{3+} (x = 1, 3, 5, 7, and 10 mol%) samples are presented in Fig. 1(a). The observed diffraction patterns are consistent with the standard (ICSD# 20838) and confirmed the formation of the orthorhombic $Sc_2Mo_3O_{12}$ phase. The same was confirmed by the Rietveld refinement of the powder XRD pattern of the pure $Sc_2Mo_3O_{12}$ sample (Fig. S1, ESI†). The obtained unit cell parameters were a = 13.24724 Å, b = 9.54709 Å, c = 9.64018 Å, and V = 1219.220 Å^3. The R_p, R_{wp}, and χ^2 values are 2.22, 3.03, and 3.77, respectively. The low R_p value of 2.22 confirmed the formation of the orthorhombic phase of $Sc_2Mo_3O_{12}$ at room temperature. The diffraction patterns of the Sm^{3+}-doped samples do not contain any impurity phase. Fig. 1(b), (c) and Fig. S2a, b (ESI†) display the SEM images of the pure $Sc_2Mo_3O_{12}$ (SMO) sample and Sm^{3+}-doped $Sc_2Mo_3O_{12}$ (SMO:5Sm and SMO:10Sm) samples, respectively. Agglomerated micron-size SMO particles with an irregular sphere-like morphology were observed in the SEM image. The extent of agglomeration increased upon Sm^{3+} doping with the formation of irregular shaped particles. Fig. S3 (ESI†) presents the FTIR spectra of the SMO:Sm samples. Vibrational bands observed in the range from 560 to 1000 cm^{-1} peaking at 800 cm^{-1} and 971 cm^{-1} can be assigned to the stretching vibrations of the MoO_4 tetrahedra.[41] The crystal structure of orthorhombic $Sc_2Mo_3O_{12}$ is presented in Fig. 1(d), showing the ScO_6 octahedron and MoO_4 lattice sites. Fig. 1(e) shows the temperature-dependent XRD patterns of SMO from 300 K to 700 K. The variation of the unit cell parameters, a, b, c, and volume (V) of $ScMo_3O_{12}$ as a function of temperature obtained by LeBail fits is shown in Fig. 1(f). The two-dimensional NTE effect was observed with contraction along the "b and c" axes, and elongation along the "a" axis.

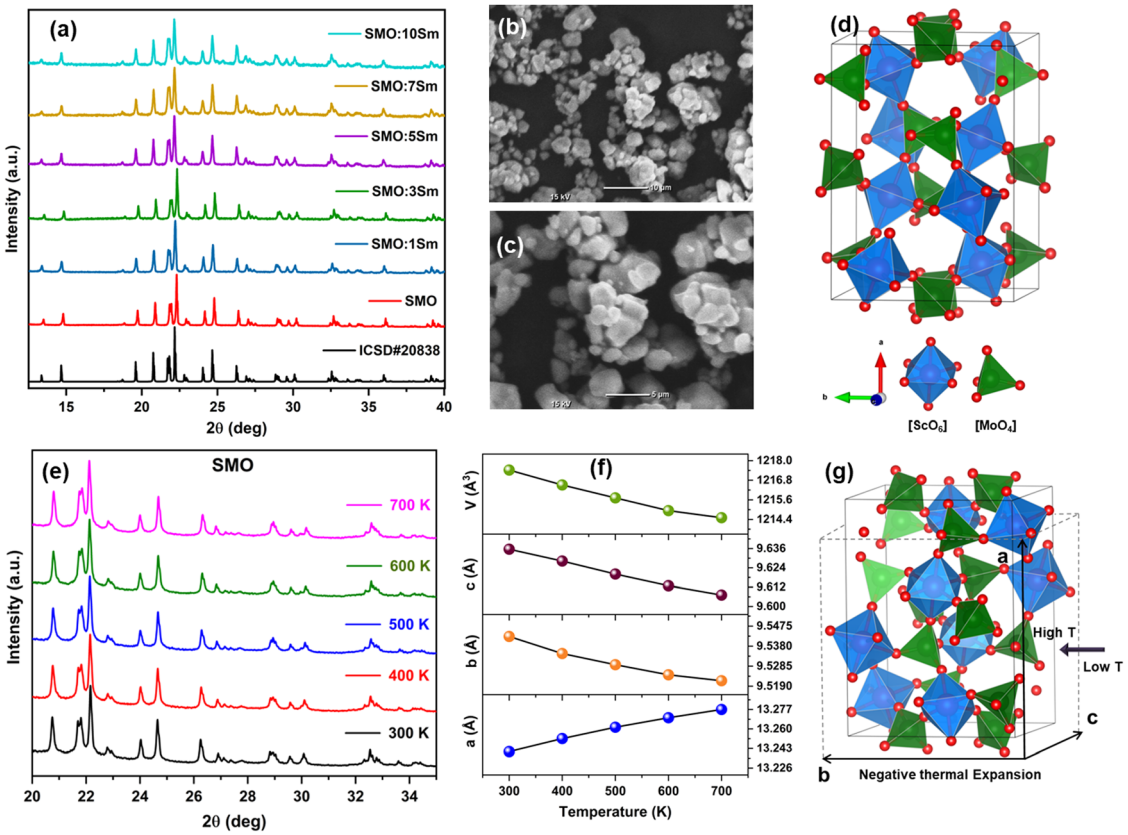

Fig. 1 (a) XRD patterns of the $Sc_2Mo_3O_{12}$:xSm^{3+} (x = 0, 1, 3, 5, 7 and 10 mol%) samples, and SEM image of SMO with scale bars at (b) 10 μm and (c) 5 μm. (d) Crystal structure of SMO. (e) High temperature-dependent XRD patterns of SMO from 300 to 700 K. (f) Changes in the unit cell parameters with temperature, and (g) schematic showing the NTE on moving from low to high temperature (T).

The volume (V) decreased with increasing temperature, and indicated NTE in the SMO lattice. The temperature-dependent XRD patterns of SMO:5Sm from 300 K to 700 K and variation of the lattice parameters as a function of temperature are shown in Fig. S4a and b (ESI†). The values of the lattice parameters of SMO and SMO:5Sm at different temperatures are tabulated in Tables S1 and S2 (ESI†), respectively. The schematic in Fig. 1(g) illustrates the unit cell contraction and two-dimensional NTE in $Sc_2Mo_3O_{12}$ with the increase in temperature. The lattice parameters increased as a result of Sm^{3+} doping in SMO due to substitution of Sc^{3+} ions by larger Sm^{3+} ions. The lattice volume expansion indicated the doping of Sm^{3+} in the SMO lattice.

3.2. EXAFS and XANES spectroscopy: oxidation state and local structure of Sm^{3+} ions

Local structural information has been obtained from the analysis of the EXAFS spectrum. The $\chi(R)$ *versus* R plots, derived from the Fourier transform of the $\chi(k)$ spectra, are illustrated in Fig. 2(a) and (b) for the Mo K-edge and Sm L3 edge, respectively. The displayed Fourier transform spectra are phase-uncorrected, leading to the coordination peak in these spectra appearing at slightly lower inter-atomic distances (R) compared to the actual bond length. To simulate the theoretical EXAFS spectrum, structural parameters were obtained from Rietveld refined XRD structures. The XAS analysis was conducted using the Demeter package, incorporating ATHENA and ARTEMIS subroutines for data processing and analysis.[42] Fitting parameters, such as the bond length and disorder factor (σ^2), were employed for EXAFS analysis. The obtained Mo and Sm EXAFS data were fitted using the Fourier transform ranges of k = 2–10 $Å^{-1}$ and 2–9 $Å^{-1}$. The fitting range used for analysis is 1–2.5 Å at both edges. The Mo K-edge EXAFS fitting (Fig. 2(a)) indicates Mo–O distances of 1.76 Å with a coordination of 4. The bond length remained the same for the doped and undoped SMO samples. The fitting results (Fig. 2(b)) at the Sm L3-edge indicate an average Sm–O coordination of 2.41 Å with a coordination number of 6. The obtained Sm–O bond lengths indicated the occupation of Sc^{3+} sites by Sm ions. The bond lengths of Sc–O and Mo–O obtained from Rietveld analysis of SMO are 1.764 Å and 2.088 Å, respectively. From EXAFS, the Mo–O and Sm–O distances were evaluated as 1.76 Å and 2.41 Å, respectively, which are in line with the XRD results. From the bond distances, the larger Sm ions occupy the Sc sites in the SMO lattice. The same was indicated by the lattice volume expansion and increase in unit cell parameter on Sm^{3+} doping from XRD data due to the substitution of Sc^{3+} ions (with an ionic radius of 0.745 Å) by the larger Sm^{3+} ions (0.958 Å ionic radius).[43] The peak on the right shoulder results from truncation effects, and includes contributions from both the first and second coordination peaks. This peak was fitted after incorporating the second coordination peak fitting at around 3.14 Å. The second coordination peak is the contribution of the Sm–Mo coordination at a distance of 3.92 Å. The asymmetric nature of the first coordination peak is evident from the disorder factor obtained for it, which reflects both structural and thermal disorder. The relatively large values (0.0102 ± 0.0025 $Å^2$) of disorder factor indicate local structural disorder around the Sm ions.

The obtained XANES spectra at the Mo K-edge and Sm L3-edge are shown in the inset of Fig. 2(a) and (b), respectively. The Mo XANES spectra of both undoped and Sm-doped SMO samples show the oxidation state of +6, as the absorption edge position coincides with the MoO_3 standard. The trivalent oxidation state of Sm can also be inferred from the inset of Fig. 2(b), as the absorption edge position is identical to that of Sm_2O_3. Hence, the XANES confirmed the presence of Sm^{3+} ions in the SMO matrix and ruled out the presence of Sm^{2+} ions.

3.3. Photoluminescence properties

Fig. 3(a) shows the PL excitation spectra of the $Sc_2Mo_3O_{12}$:xSm (x = 1, 3, 5, 7, and 10 mol%) phosphors monitored at the emission wavelength of 647 nm. The broadband in the 250–325 nm region is the charge transfer band (CTB) originated from the $O^{2-} \rightarrow Sm^{3+}$ charge transfer. The CTB band is composed of bands peaking at ~270 and 300 nm, which can be ascribed to charge transfer from O^{2-} (2p) → Sm^{3+} (4f) and $O^{2-} \rightarrow Mo^{6+}$ in MoO_4^{2-}, respectively. The energy level diagram of the Sm^{3+} ions and the proposed mechanism of charge

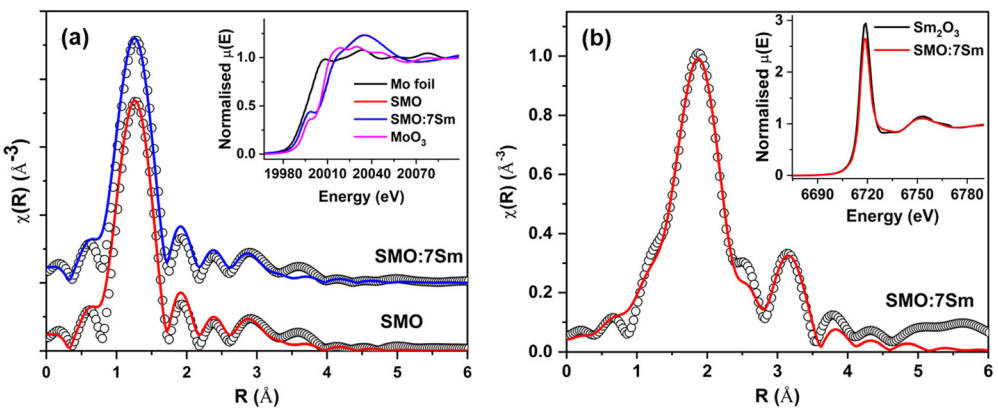

Fig. 2 (a) Fourier-transformed EXAFS spectra (scatter points) and their respective fittings (solid line) at the Mo K-edge. The inset shows the normalised XANES spectra at the Mo K-edge, along with the Mo metal foil and MoO_3 standards. (b) Fourier-transformed EXAFS spectra (scatter points) and their respective fittings (solid line) at the Sm L3-edge. The inset shows the normalised XANES spectra at the Sm L3-edge, along with the Sm_2O_3 standard.

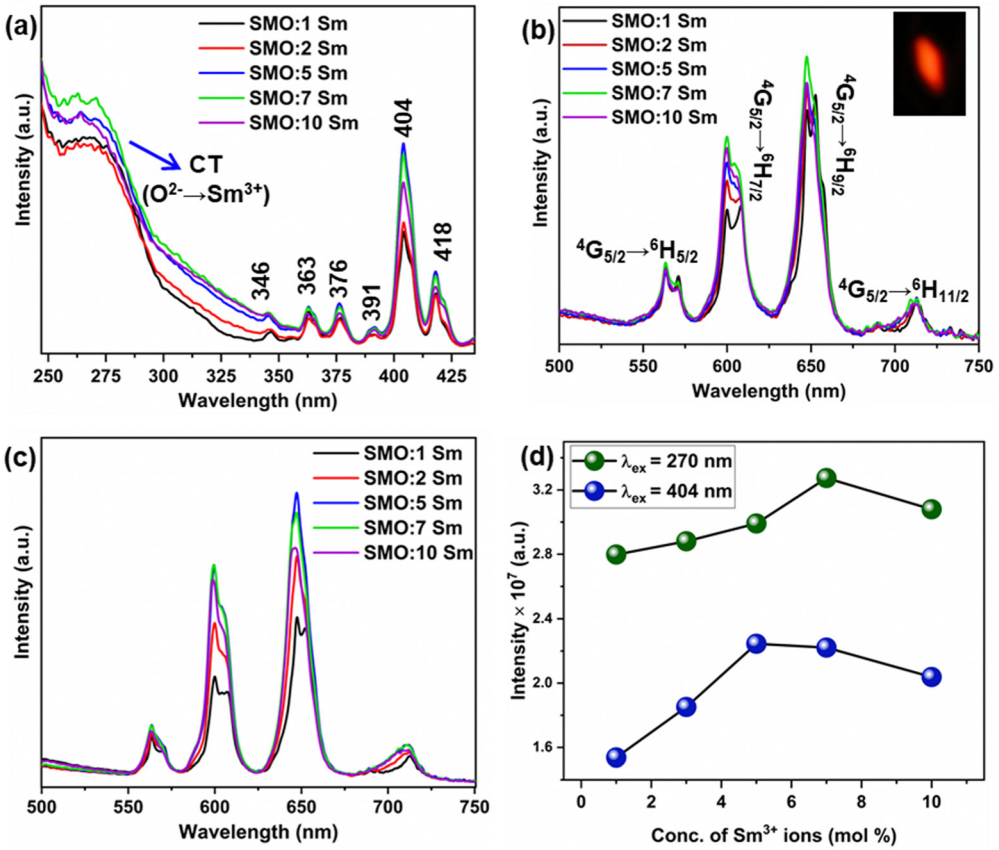

Fig. 3 (a) PL excitation spectra of the $Sc_2Mo_3O_{12}$:xSm^{3+} (x = 0, 1, 3, 5, 7 and 10 mol%) phosphors monitored at 647 nm emission. (b) PL emission spectra of the SMO:Sm samples at 270 nm excitation (inset shows the emission photograph of SMO:5Sm). (c) PL emission spectra of the SMO:Sm samples at 404 nm excitation, and (d) variation in the PL intensity with concentration of Sm^{3+} ions.

transfer (CT) from MoO_4^{2-} to Sm^{3+} ions are shown in Scheme 1. The intra 4f–4f transitions of the Sm^{3+} ions were observed beyond 330 nm, which can be assigned to the $^6H_{5/2} \rightarrow {}^4D_{7/2}$, $^4D_{9/2}$ (346 nm), $^6H_{5/2} \rightarrow {}^4P_{3/2}$, $^4D_{3/2}$ (363 nm), $^6H_{5/2} \rightarrow {}^4L_{17/2}$, $^6P_{7/2}$, $^4D_{1/2}$ (376 nm), $^6H_{5/2} \rightarrow {}^4P_{3/2}$, $^4F_{7/2}$, $^4L_{13/2}$ (391 nm and 404 nm), $^6H_{5/2} \rightarrow {}^6P_{5/2}$ (418 nm) transitions, respectively (Scheme 1).[39] The CT band at 270 nm and the most intense absorption peak at 404 nm were used to study the emission of the Sm^{3+} ions. The absorption efficiency of the Sm^{3+} ions in the UV and near-UV region is low, but the MoO_4^{2-} group can sensitize Sm^{3+} emissions *via* charge transfer transition. Thus, SMO:Sm phosphors can be excited by a wide range of excitations in the UV and near-UV regions, and by blue light to develop a promising orange-red light emitting phosphor for developing WLEDs. Fig. 3(b) and (c) presents the PL emission spectra of the SMO:Sm samples at the excitation wavelengths of 270 nm and 404 nm, respectively. The PL emission intensity is strong for the 270 nm CT excitation in comparison to the 404 nm excitation. The PL emission spectra exhibit the four typical sharp bands of Sm^{3+}, peaking at 563 ($^4G_5 \rightarrow {}^6H_{5/2}$), 600 ($^4G_5 \rightarrow {}^6H_{7/2}$), 647 ($^4G_5 \rightarrow {}^6H_{9/2}$), and 713 nm ($^4G_5 \rightarrow {}^6H_{11/2}$), respectively.[44] The $^4G_5 \rightarrow {}^6H_{5/2}$ transition (563 nm) is purely magnetic-dipole (MD) allowed, whereas the $^4G_5 \rightarrow {}^6H_{7/2}$ transition (600 nm) is both MD and electric-dipole (ED) allowed. Meanwhile, $^4G_5 \rightarrow {}^6H_{9/2}$ (647 nm) is a purely ED-allowed transition.[10,45] In all of the SMO:Sm samples, the EDT emission is more intense than MDT, which indicated the asymmetric local structure of the Sm^{3+} ions. The same conclusion was indicated by the local structural disorder around the Sm ions observed in the EXAFS results.

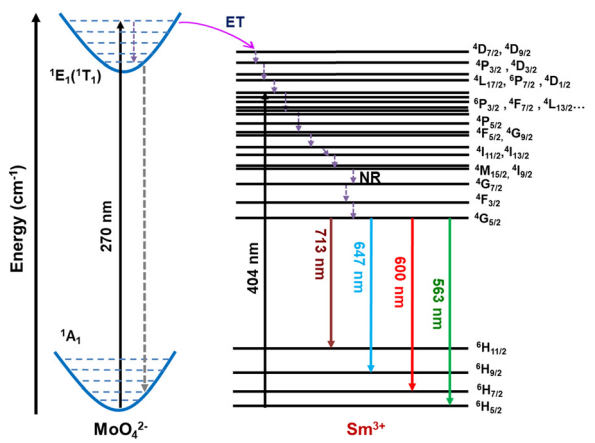

Scheme 1 Schematic showing the energy level diagram of Sm^{3+} and charge transfer transition between the MoO_4^{2-} and Sm^{3+} ions.

In Fig. 3(a), the CT band increased in intensity with increased doping content of Sm^{3+} ions up to 7 mol% of Sm^{3+} ions. The PL

emission intensity under CTB excitation (λ_{ex} = 270 nm) initially increased with the increment in Sm^{3+} doping concentration up to x = 7 mol%,and decreased upon further increase in the Sm^{3+} concentration. This may be due to the non-radiative energy loss between the Sm^{3+}–Sm^{3+} ions known as concentration quenching. The emission image of the SMO:5Sm sample captured by camera is presented in the inset of Fig. 3(b). Under 4f–4f excitation (λ_{ex} = 404 nm), the PL emission intensity increased with the increase in Sm^{3+} doping amounts up to x = 5 mol%. Further increase in the Sm^{3+} concentration led to decreased PL intensity. The variation of the integrated emission intensities under CTB and 4f excitation is illustrated by Fig. 3(d). The CT process from MoO_4^{2-} to Sm^{3+} can take place after CTB excitation with 270 nm. The UV excitation energy absorbed by the MoO_4^{2-} group (O2p) is transferred from the $^1E_1$ ($^1T_1$) excited state to the $^4D_{7/2}$ state of the Sm^{3+} ions.[2] The Sm^{3+} emissions occur from the radiative decay from the $^4G_{5/2}$ excited state to the $^6H_{J/2}$ level (J = 5, 7, 9 and 11).[46] The non-radiative processes (NR) resulted in the filling of electrons in the $^4G_{5/2}$ excited state.

The luminescence decay profiles of the Sm^{3+}-doped SMO phosphors monitored at the 647 nm emission of the Sm^{3+} ions upon CTB (270 nm) and 4f–4f excitation (404 nm) are shown in Fig. 4(a) and (b), respectively. The decay curves were fitted using the biexponential decay function:

$$I(t) = I_0 + A_1 e^{-t/\tau_1} + A_2 e^{-t/\tau_2} \quad (1)$$

where $I(t)$ and I_0 represent the emission intensity at time 't' and at zero offset, A_1 and A_2 are constants, and τ_1 and τ_2 are the slow and fast lifetime components, respectively. The lifetime values of the Sm^{3+}-doped SMO phosphors under different excitation wavelengths are summarized in Table S3 (ESI†). The biexponential decay behavior indicated two different de-excitation pathways for the Sm^{3+} ions in excited levels. The variations in the average lifetime (τ_{av}), slow and fast lifetime components, and percentage of τ_1 and τ_2 as a function of Sm^{3+} doping concentration under CTB and 404 nm excitation are shown in Fig. 4(c) and (d), respectively. It was observed that the average lifetime decreased with the increase in the Sm^{3+} doping content, which can be ascribed to concentration quenching. The higher Sm^{3+} doping amounts may induce non-radiative energy transfer between the Sm^{3+}–Sm^{3+} pairs, as suggested by the decrease in the radiative lifetime of Sm^{3+} ions at higher concentration and the increase in the percentage of the fast lifetime component.

3.4. Temperature-dependent photoluminescence properties

Fig. 5(a) presents the temperature-dependent PL emission spectra of the SMO:5Sm phosphor excited at 280 nm. Above 298 K, the SMO:5Sm phosphor exhibits the anti-thermal quenching of Sm^{3+} luminescence and significant enhancement in the PL intensity is observed with the increasing temperature. At 433 K, the emission intensity of Sm^{3+} reaches 591% of the initial intensity at 298 K (Fig. 5(b)). The enhancement can be explained by the increase in the structural rigidity due to the NTE of the SMO matrix above room temperature, as confirmed by the temperature-dependent XRD data. This resulted in a decrease in thermal non-radiative losses at elevated temperatures.

The NTE in the $Sc_2Mo_3O_{12}$ matrix can be attributed to perpendicular transverse vibrations of bridging O atoms in

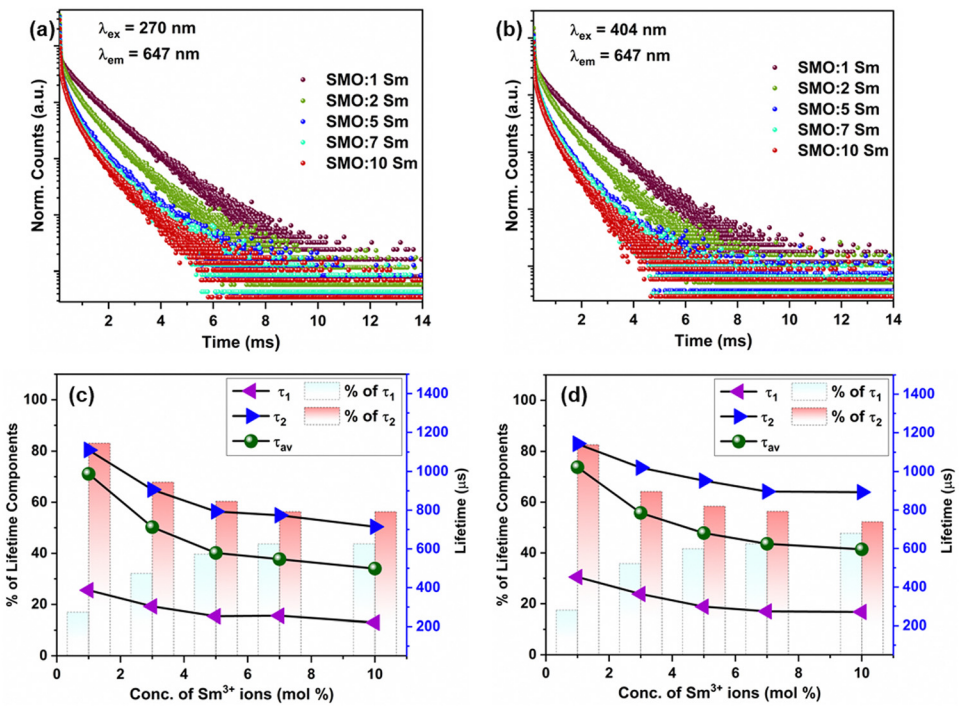

Fig. 4 Decay profiles of the $Sc_2Mo_3O_{12}$:xSm^{3+} (x = 0, 1, 3, 5, 7 and 10 mol%) phosphors monitored at λ_{em} = 647 nm upon excitation at (a) λ_{ex} = 270 nm and (b) λ_{ex} = 404 nm, and (c), (d) variation of the lifetime values as a function of the Sm^{3+} doping concentration for λ_{ex} = 270 nm and λ_{ex} = 404 nm, respectively.

the Sc–O–Mo bonds, which is assisted by polyhedron tilting and 3D couple twisting with an increase in temperature.[20,21,47] These structural motions result in a decrease of the Sm–Mo distance and Sm–O–Mo bond angle, which strengthen the MoO_4^{2-}-to-Sm^{3+} energy transfer.[3] Consequently, the enhanced CTB absorption between O^{2-} and Sm^{3+} at elevated temperatures induced by NTE led to thermally enhanced luminescence of Sm^{3+} ions. The CIE color coordinates illustrate the emission shift from a reddish-orange color with CIE (0.53, 0.45) at room temperature to a red color with CIE (0.67, 0.34) at elevated temperatures (Fig. 5(c)). Overall, the emission enhancement in the SMO:5Sm phosphor was attained in a wide temperature range of 298–433 K under strong CTB excitation. The anti-thermal quenching of Sm^{3+} luminescence at CTB excitation unveiled the impact of NTE in achieving thermally enhanced emission.

3.5. Impact of the phase transition on photoluminescence

As discussed in the introduction, we studied the temperature-dependent PL to investigate the effect of the structural phase transition of $Sc_2Mo_3O_{12}$ on the luminescence under cryogenic conditions. We investigated the phase transition in the SMO:5Sm sample by using differential scanning calorimetry (DSC) measurements (Fig. S5, ESI†) in the range of −20 °C (253 K) to −120 °C (150 K). We observed a significant change in heat flow around −80 °C, which marked the onset of the phase transition in SMO:5Sm that occurs in the range from −80 °C to −100 °C. This observation is in line with the literature discussed above. To further confirm the phase transition of the $Sc_2Mo_3O_{12}$ phase from the monoclinic to orthorhombic phase from 80 K to 300 K, we performed temperature-dependent Raman measurements for the SMO:5Sm sample. The monoclinic-to-orthorhombic phase transformation will result in a decrease in the number of vibrational modes.[48] The Raman spectra contain the stretching bands of Mo–O bonds above 800 cm^{-1}. However, the peak at 1000 cm^{-1} diminished with an increase in temperature from 80 to 300 K (Fig. S6, ESI†). This suggested that the complete phase transition occurs on heating the SMO:5Sm sample from 77 to 200 K, and only the orthorhombic phase is present at room temperature.[49]

The monoclinic phase shows a temperature-dependent positive thermal expansion and the NTE property is present in the orthorhombic phase. Fig. 6(a) presents the temperature-dependent PL excitation spectra of the SMO:5Sm phosphor monitored at the 647 nm ($^4G_5 \rightarrow {}^6H_{9/2}$) emission of Sm^{3+}. With the increase in temperature, the CTB significantly decreased in intensity due to the thermally induced lattice expansion in the monoclinic phase, which may reduce the CT ($MoO_4^{2-} \rightarrow Sm^{3+}$) efficiency. In contrast, the intra 4f–4f transitions in the excitation spectra exhibit weak thermal quenching relative to CTB. Thus, the phase transition-induced modulation in the lattice matrix severely affected the charge transfer from $MoO_4^{2-} \rightarrow Sm^{3+}$ ions.

The temperature-dependent PL emission spectra of the SMO:5Sm phosphor upon CTB (270 nm) and 404 nm excitation are shown in Fig. 6(b) and (c), respectively. The variation in the excitation and emission intensities is well illustrated by the respective contour plots as a function of temperature (Fig. 6(d)–(f)). Interestingly, a strong broadband emission of the MoO_4^{2-} group is observed at 80 K (−193 °C), along with the sharp emissions of the Sm^{3+} ions. The excitation spectra acquired at the host emission (520 nm) is presented in Fig. S7 (ESI†), which exhibits the $O^{2-} \rightarrow Mo^{6+}$ charge transfer bands in the region of 250 to 325 nm. As can be seen from the emission and excitation spectra (Fig. 6(b) and Fig. S7, ESI†), the host emission and CTB absorption is observable up to 180 K, and quenched completely at room temperature. The same is clearly demonstrated by the emission contour plots for the CTB excitation in Fig. 6(e), where the host emission completely diminished above 180 K. Since the phase transition occurs around 180 K, we can attribute the host emission as occurring mainly in the monoclinic phase of SMO. The comparison of the excitation spectrum monitored at the host emission (520 nm) and Sm^{3+} emission (647 nm) at 80 K is shown in Fig. S8 (ESI†).

The Sm^{3+} emission undergoes thermal quenching from 80 to 300 K, which may be a result of decreased CTB intensity with increasing temperature. Additionally, the increased probability of non-radiative transitions is due to the intensified thermal vibration of the monoclinic SMO lattice at elevated temperature. These thermally activated phonons are the cause for the loss of Sm^{3+} and host emission. Upon 404 nm excitation, the PL intensity decreased at a relatively much lower rate and no changes in the spectral profile of Sm^{3+} emissions were noticeable

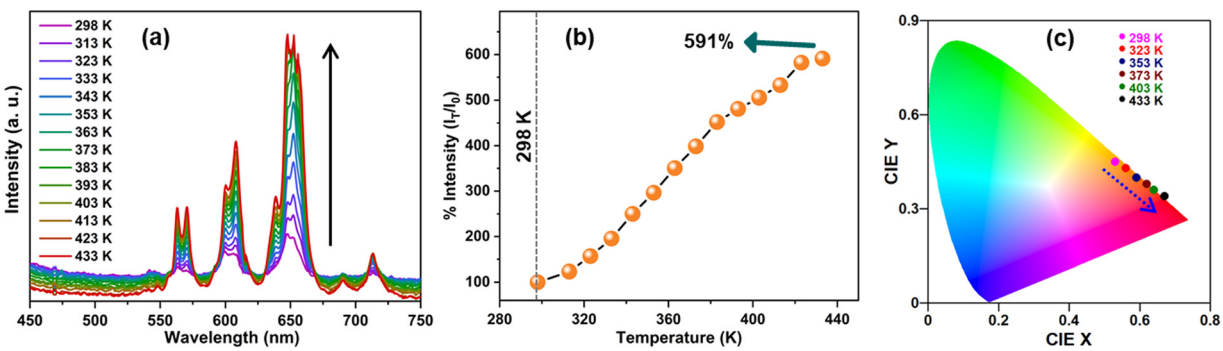

Fig. 5 (a) Temperature-dependent PL emission spectra of the SMO:5Sm sample excited at 280 nm in the range of 298 to 433 K. (b) Variation of the integrated PL emission intensities of the SMO:5Sm sample as a function of temperature. (c) Change in the CIE color coordinates of the Sm^{3+} emission with an increase in temperature.

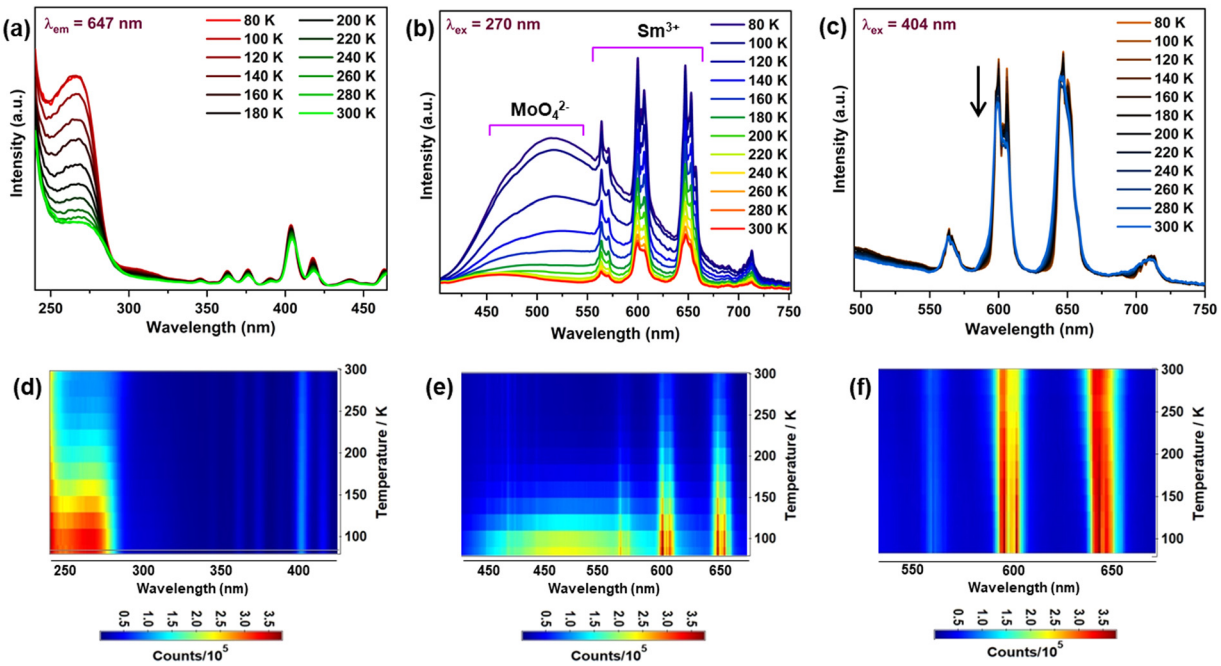

Fig. 6 (a) Temperature-dependent PL excitation spectra of SMO:5Sm monitored at 647 nm emission in the range of 80 to 300 K. (b) Temperature-dependent PL emission spectra excited at 270 nm excitation. (c) Temperature-dependent PL emission spectra of the SMO:5Sm sample at 404 nm excitation. (d)–(f) Temperature-dependent contour plots showing the variation in the excitation bands (λ_{em} = 647 nm), emission intensity under 270 and 404 nm as a function of temperature, respectively.

with increasing temperature (Fig. 6(c)). These findings suggest that the displacive nature of the phase transition in the SMO matrix has a minor effect on the emission profile of the Sm^{3+} ions when excited at the 4f–4f transition (404 nm).

To further understand the impact of the phase transition on luminescence, temperature-dependent decay profiles of the Sm^{3+} emission at 647 nm were acquired under CTB and 404 nm excitation, as shown in Fig. 7(a) and (b), respectively. It can be seen that the lifetime values show a decreasing trend with the increase in temperature from 80 to 300 K. Fig. 7(c) shows the variation in lifetime values as a function of temperature for CTB and 404 nm excitation. It is notable that the lifetime values showed different behaviors below 150 K, followed by a gradual decrease up to 260 K, and then an abrupt decrease in lifetime from 260 K to 300 K. The initial region (<150 K) has the characteristics of the monoclinic phase, and the changes in lifetime (~160 K) were induced by the onset of the orthorhombic phase formation. The EDT emission is hypersensitive to minute changes in the local structure of Sm^{3+} ions, and the sudden rise in the lifetime at 160 K indicates small changes in the local surrounding of the Sm^{3+} ions. As concluded by Young *et al.*,[26] a mixed proportion of monoclinic and orthorhombic phases in the temperature range of 160 K to 220 K resulted in the observed changes in the lifetimes. Above 260 K, the sharp dip in lifetime values can be assigned to the increase in non-radiative processes induced by thermally activated phonons. The decay curves for the host emission for the MoO_4^{2-} group at 520 nm under CTB excitation are presented in Fig. S9 (ESI†), and the lifetime of the MoO_4^{2-} emission decreased from 258 μs to 16 μs from 80 K to 200 K.

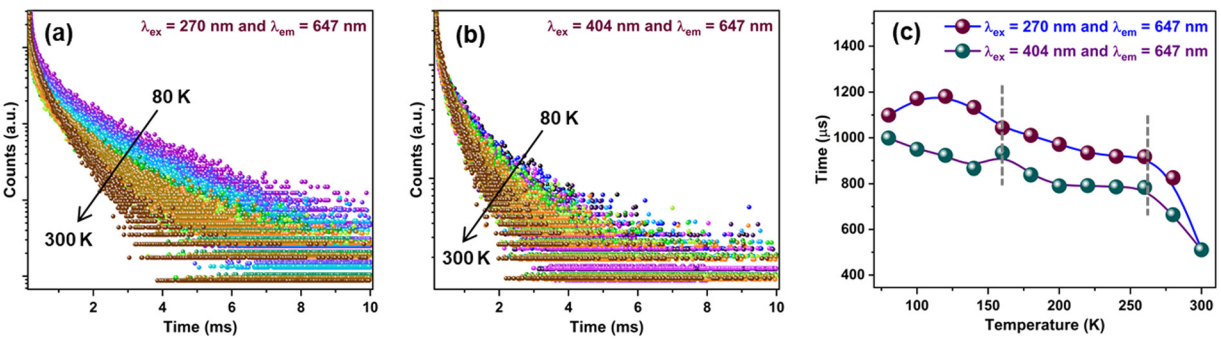

Fig. 7 Temperature-dependent decay profiles of the SMO:5Sm sample for 647 nm emission excited at (a) 270 nm and (b) 404 nm in the range of 80 to 300 K, respectively. (c) Variation of the lifetime values as a function of temperature.

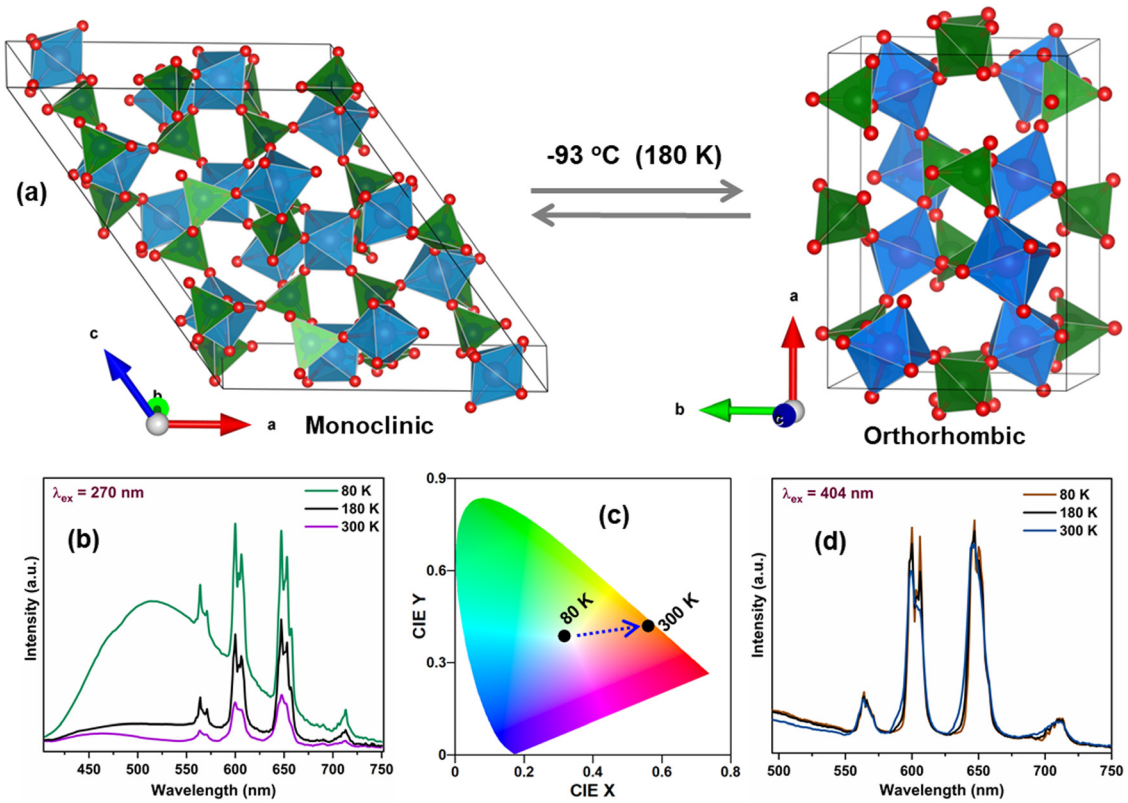

Fig. 8 (a) Schematic illustrating structural changes with reversible phase transition from the monoclinic to orthorhombic phase of SMO with temperature. (b) Comparison of emission when excited at 270 K. (d) Changes in CIE color coordinates with temperature, and (d) comparison of emission when excited at 404 K.

The schematic in Fig. 8(a) illustrates the reversible phase transition of SMO from the monoclinic to orthorhombic phase at −93 °C with temperature.[26] The significant changes in the emission spectra and CIE color coordinates from 80 K to 300 K when excited at 270 nm are shown in Fig. 8(b) and (c) depicting the color being tuned from white to red. On the other hand, Fig. 8(d) clearly shows the minuscule changes in the emission of Sm^{3+} under 404 nm excitation in the same temperature range.

3.6. The prototype pc-LEDs for lighting applications

A prototype white-LED was fabricated by pasting a mixture of optimized red-emitting $Sc_2Mo_3O_{12}:Sm^{3+}$, blue-emitting commercial BAM:Eu^{2+}, and green-emitting commercial CMA:Tb^{3+} phosphors onto a 280 nm UV LED chip operating at a voltage of 12 V and current of 2 A. Herein, two different ratios of the phosphor mixture were taken for the white LED evaluations, as displayed in Fig. 9. The corresponding electroluminescence (EL) spectra for the white LEDs fabricated with two different combinations are given in Fig. 9(a) and (b), and the corresponding CIE color diagram is shown in Fig. 9(c). As shown in Fig. 9(a), the obtained white-LED with the RGB mixing ratio of 1 : 1 : 3 displays a cool white light, with a luminous efficacy of radiation (LER) of 113 lm W^{-1}, correlated color temperature (CCT) of 6043 K, color rendering index (Ra) of 57, and CIE chromaticity coordinates (0.31, 0.42). This cool white light is also clearly noticeable from the inset of Fig. 9(a), which displays the digital image of the fabricated pc-LED. When the RGB mixing ratio was tuned to 1 : 1 : 7, the resultant pc-LED displayed a warm white light with the LER of 96 lm W^{-1} CCT of 5408 K, Ra of 84, and CIE (0.33, 0.32). This resultant white LED prototype is demonstrated in the inset of Fig. 9(b), and the high Ra of the fabricated white LED is the ultimate requirement for high-definition lighting.

3.7. Fabrication of the red pc-LED for indoor plant growth applications

To further evaluate the potential of the optimized $Sc_2Mo_3O_{12}:Sm^{3+}$ red phosphor, two red pc-LEDs were fabricated by combining this optimized red phosphor with a 280 nm UV-LED chip and a 410 nm blue LED chip individually, both operated at a voltage of 12 V and current of 2 A. The corresponding EL spectra are shown in Fig. 10(a) and (b), respectively. The effective red emission with moderate color purity is visible from the relevant CIE diagram for the 280 nm excitation-based red pc-LED that has CIE coordinates of (0.51, 0.23), as shown in the inset of Fig. 10(a). An efficient red phosphor with such characteristics is very useful not only in making white LEDs with improved color rendering (Ra), but also can be efficiently utilized for display applications.

In Fig. 10(b), an efficient plant growth application has also been studied for the red pc-LED fabricated by combining the optimized $Sc_2Mo_3O_{12}:Sm^{3+}$ phosphor with a 410 nm blue LED

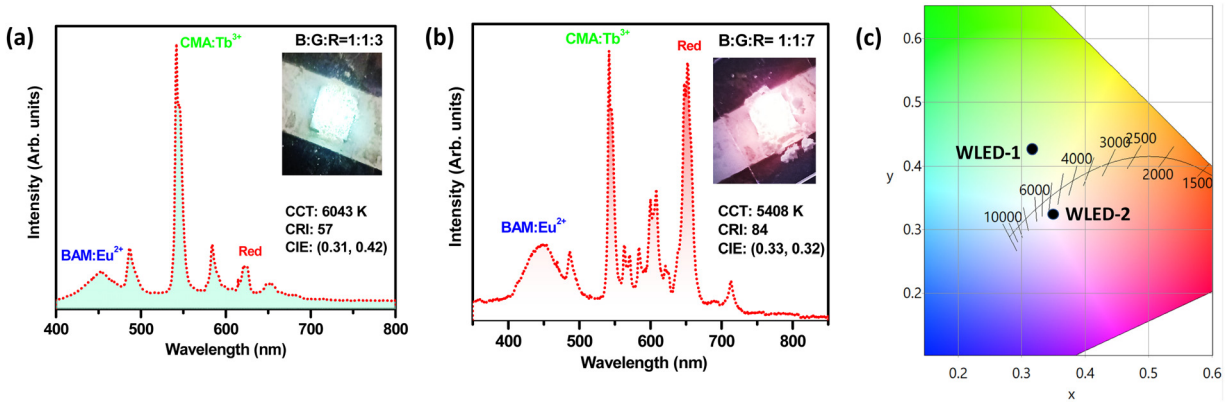

Fig. 9 The electroluminescence spectra for the prototype white LED with the blue, green, and red phosphors in the ratios of (a) 1 : 1 : 3 and (b) 1 : 1 : 7. The insets (a) and (b) show the digital images for the corresponding LEDs. (c) The CIE color diagram for the white LEDs in different mixing ratios.

chip. As depicted in Fig. 10(b), the electroluminescence spectrum of the above pc-LED was plotted along with the absorption spectra of the plant pigment phytochrome P_R, which has the absorption maxima at ~660 nm. There is a significant overlap between the absorption spectrum of phytochrome, and the red emission band of the pc-LED has been observed in Fig. 10(b). This promising overlap indicates that the phosphor has the potential to be an efficient artificial light source for cultivating indoor plant growth.[27]

4. Conclusion

Herein, we report a series of $Sc_2Mo_3O_{12}:Sm^{3+}$ (SMO:Sm^{3+}) reddish-orange emitting phosphors with intense charge transfer from the MoO_4^{2-} group in the host SMO ($O^{2-} \rightarrow Sm^{3+}$). This enhanced the absorption of UV and near-UV light by Sm^{3+}, along with intra 4f–4f blue light excitation. The temperature-dependent XRD studies investigated NTE in SMO from 300 K to 700 K. The NTE resulted in the anti-TQ performance of SMO:Sm^{3+} in a wide temperature range from 298 to 433 K due to the improved structural rigidity and charge transfer absorption. We observed a ~6-fold enhancement in Sm^{3+} emission, and 591% of Sm^{3+} intensity at room temperature was retained at 433 K. Two prototypes for WLED and indoor plant growth were demonstrated by the fabrication of the SMO:Sm^{3+} phosphor onto UV and 410 nm LED chips, respectively. The WLED offers a high CRI of 84, CIE (0.33, 0.32), and CCT of 5408 K, and high luminous efficacy of 113 lm W^{-1}. The red emission band of the pc-LED overlaps with the absorption spectrum of phytochrome, P_R, and presents an efficient artificial light source for cultivating indoor plant growth. Furthermore, we investigated the temperature-dependent cryogenic PL properties, which revealed that the phase transition has a minor impact on the Sm^{3+} local structure and Sm^{3+} luminescence profile. This is the first report which explores green MoO_4^{2-} emission in the monoclinic $Sc_2Mo_3O_{12}$ phase at −193 °C, which diminished in the orthorhombic phase. This work reports a promising Sm^{3+}-activated phosphor for lighting and indoor plant growth LEDs with anti-TQ performance.

Data availability

The data supporting this article have been included as part of the ESI.†

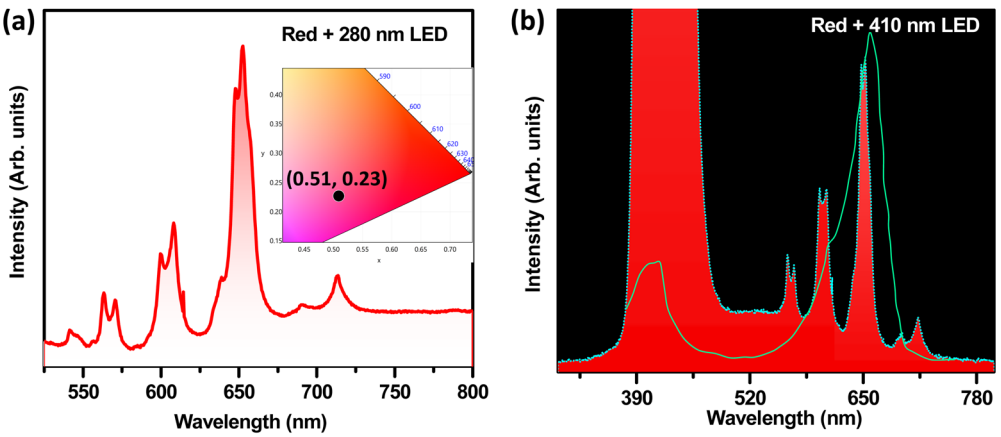

Fig. 10 (a) The electroluminescence spectra for the $Sc_2Mo_3O_{12}:Sm^{3+}$ sample excited with 280 nm LED. The inset shows the chromaticity diagram for the same sample showing the CIE coordinates. (b) The electroluminescence spectra for the $Sc_2Mo_3O_{12}:Sm^{3+}$ sample excited with 410 nm LED, along with the absorption spectra of the plant pigment phytochrome P_R.

Conflicts of interest

There are no conflicts to declare.

Acknowledgements

A. Balhara and Santosh K. Gupta would like to thank Dr Chiranjit Nandi, BARC, for help in high temperature-dependent X-ray measurements. We would also like to acknowledge Dr Manoj Kumar Gupta, AMPRI, for SEM analysis, Kanaklata Pandey, BARC, for help in DSC measurements, and Dr Ashish Kumar Mishra from IIT BHU for temperature-dependent Raman measurements. This research is funded by Government of India through Department of Atomic Energy (DAE).

References

1 P. Dang, W. Wang, H. Lian, G. Li and J. Lin, How to obtain anti-thermal-quenching inorganic luminescent materials for light-emitting diode applications, *Adv. Opt. Mater.*, 2022, **10**(6), 2102287.
2 S. Hariyani and J. Brgoch, Spectral design of phosphor-converted LED lighting guided by color theory, *Inorg. Chem.*, 2021, **61**(10), 4205–4218.
3 F. Jahanbazi and Y. Mao, Impact of negative thermal expansion on thermal quenching of luminescence of $Sc_2Mo_3O_{12}$:Eu^{3+}, *Chem. Mater.*, 2022, **34**(23), 10538–10547.
4 J. Li, J. Yan, D. Wen, W. U. Khan, J. Shi, M. Wu, Q. Su and P. A. Tanner, Advanced red phosphors for white light-emitting diodes, *J. Mater. Chem. C*, 2016, **4**(37), 8611–8623.
5 J. Liao, M. Wang, F. Lin, Z. Han, B. Fu, D. Tu, X. Chen, B. Qiu and H.-R. Wen, Thermally boosted upconversion and downshifting luminescence in $Sc_2(MoO_4)_3$:Yb/Er with two-dimensional negative thermal expansion, *Nat. Commun.*, 2022, **13**(1), 2090.
6 A. Balhara, S. K. Gupta, M. Abraham, B. Modak, S. Das, C. Nayak, H. V. Annadata and M. Tyagi, Trap engineering through chemical doping for ultralong X-ray persistent luminescence and anti-thermal quenching in Zn_2GeO_4, *J. Mater. Chem. C*, 2024, **12**(5), 1728–1745.
7 S. K. Gupta, R. M. Kadam and P. K. Pujari, Lanthanide spectroscopy in probing structure-property correlation in multi-site photoluminescent phosphors, *Coord. Chem. Rev.*, 2020, **420**, 213405.
8 X. Geng, Y. Xie, S. Chen, J. Luo, S. Li, T. Wang, S. Zhao, H. Wang, B. Deng and R. Yu, Enhanced local symmetry achieved zero-thermal-quenching luminescence characteristic in the Ca_2InSbO_6:Sm^{3+} phosphors for w-LEDs, *Chem. Eng. J.*, 2021, **410**, 128396.
9 Z. Leng, H. Bai, Q. Qing, H. He, J. Hou, B. Li, Z. Tang, F. Song and H. Wu, A zero-thermal-quenching blue phosphor for sustainable and human-centric WLED lighting, *ACS Sustainable Chem. Eng.*, 2022, **10**(33), 10966–10977.
10 Y. Yang, F. Li, Y. Lu, Y. Du, L. Wang, S. Chen, X. Ouyang, Y. Li, L. Zhao and J. Zhao, $CaGdSbWO_8$:Sm^{3+}: A deep-red tungstate phosphor with excellent thermal stability for horticultural and white lighting applications, *J. Lumin.*, 2022, **251**, 119234.
11 S. K. Gupta, K. Sudarshan and R. M. Kadam, Optical nanomaterials with focus on rare earth doped oxide: A Review, *Mater. Today Commun.*, 2021, **27**, 102277.
12 Y. Kuang, Y. Li, B. Chen, S. Zhao, M. Chen, S. Lian and J. Zhang, Regulating anti-thermal quenching to zero thermal quenching for highly efficient blue-emitting Eu^{2+}-doped K-beta-alumina phosphors, *J. Mater. Chem. C*, 2023, **11**(17), 5874–5881.
13 T. Tian, Z. Wang, C. Mao, M. Chen, Y. Chu and Y. Li, Structure, luminescence properties and anti-thermal quenching of a novel Eu^{3+}-activated red phosphor based on the negative thermal expansion material $In_{0.5}Sc_{1.5}(MoO_4)_3$., *J. Alloys Compd.*, 2024, **973**, 172887.
14 P. Dang, G. Li, X. Yun, Q. Zhang, D. Liu, H. Lian, M. Shang and J. Lin, Thermally stable and highly efficient red-emitting Eu^{3+}-doped $Cs_3GdGe_3O_9$ phosphors for WLEDs: non-concentration quenching and negative thermal expansion, *Light: Sci. Appl.*, 2021, **10**(1), 29.
15 B. Fu, H. Yan, R. Li, Z. Liao, B. Qiu, G. Gong, H. Huang, Y. Sun, H.-R. Wen and J. Liao, Simultaneously tuning the luminescent color and realizing an optical temperature sensor by negative thermal expansion in $Sc_2(WO4)_3$:Tb/Eu phosphors, *Dalton Trans.*, 2024, **53**(2), 798–807.
16 H. Liu, C. Zhang, W. Sun, Z. Zhang, M. Zhou, W. Wang, X. Chen and X. Zeng, Scandium molybdate nanofibers with negative thermal expansion for fabricating composites with controllable coefficients of thermal expansion, *ACS Appl. Nano Mater.*, 2020, **3**(7), 7130–7135.
17 T. A. Mary, J. Evans, T. Vogt and A. Sleight, Negative thermal expansion from 0.3 to 1050 Kelvin in ZrW_2O_8, *Science*, 1996, **272**(5258), 90–92.
18 M. Wu, X. Liu, D. Chen, Q. Huang, H. Wu and Y. Liu, Structure, Phase Transition, and Controllable Thermal Expansion Behaviors of $Sc_{2-x}Fe_xMo_3O_{12}$, *Inorg. Chem.*, 2014, **53**(17), 9206–9212.
19 F. Jahanbazi, N. Dimakis and Y. Mao, Interplay of consecutive energy transfer and negative thermal expansion property for achieving superior anti-thermal quenching luminescence, *Adv. Opt. Mater.*, 2024, **12**(1), 2301219.
20 H. Liu, F. Huang, A. R. H. Alzakree and Z. Zhang, Fabrication, negative thermal expansion and optical properties of scandium molybdate thin films, *J. Mater. Sci.*, 2022, **57**(36), 17162–17171.
21 H. Liu, N. Zhang and Z. Zhang, Investigating negative thermal expansion property of decahedral $Sc_2Mo_3O_{12}$ prepared via hydrothermal method, *Solid State Sci.*, 2022, **132**, 106961.
22 H. Zou, B. Chen, Y. Hu, Q. Zhang, X. Wang and F. Wang, Simultaneous enhancement and modulation of upconversion by thermal stimulation in $Sc_2Mo_3O_{12}$ crystals, *J. Phys. Chem. Lett.*, 2020, **11**(8), 3020–3024.
23 C. P. Romao, S. P. Donegan, J. Zwanziger and M. A. White, Relationships between elastic anisotropy and thermal expansion in $A_2Mo_3O_{12}$ materials, *Phys. Chem. Chem. Phys.*, 2016, **18**(44), 30652–30661.

24 J. S. Evans and T. Mary, Structural phase transitions and negative thermal expansion in $Sc_2(MoO_4)_3$, *Int. J. Inorg. Mater.*, 2000, **2**(1), 143–151.
25 Y. Yamamura, S. Ikeuchi and K. Saito, Characteristic phonon spectrum of negative thermal expansion materials with framework structure through calorimetric study of $Sc_2M_3O_{12}$ (M = W and Mo), *Chem. Mater.*, 2009, **21**(13), 3008–3016.
26 L. Young, P. T. Alvarez, H. Liu and C. Lind, Extremely low temperature crystallization in the $A_2Mo_3O_{12}$ family of negative thermal expansion materials, *Eur. J. Inorg. Chem.*, 2016, (8), 1251–1256.
27 R. T. Parayil, S. K. Gupta, M. Abraham, S. Das, S. S. Pitale, K. Sudarshan and M. Mohapatra, Ultra-bright and thermally stable deep red emitting doped yttrium zirconate nanoparticles for tunable white LEDs and indoor plant growth, *Mater. Adv.*, 2023, **4**(22), 5594–5604.
28 S. He, F. Xu, T. Han, Z. Lu, W. Wang, J. Peng, F. Du, F. Yang and X. Ye, A Mn^{4+}-doped oxyfluoride phosphor with remarkable negative thermal quenching and high color stability for warm WLEDs, *Chem. Eng. J.*, 2020, **392**, 123657.
29 Z. Zhou, N. Zhou, M. Xia, M. Yokoyama and H. B. Hintzen, Research progress and application prospects of transition metal Mn^{4+}-activated luminescent materials, *J. Mater. Chem. C*, 2016, **4**(39), 9143–9161.
30 S. K. Gupta, M. Abdou, J. P. Zuniga, A. A. Puretzky and Y. Mao, Samarium-Activated $La_2Hf_2O_7$ Nanoparticles as Multifunctional Phosphors, *ACS Omega*, 2019, **4**(19), 17956–17966.
31 S. K. Gupta, P. S. Ghosh, A. K. Yadav, S. N. Jha, D. Bhattacharyya and R. M. Kadam, Origin of blue-green emission in α-$Zn_2P_2O_7$ and local structure of Ln^{3+} ion in α-$Zn_2P_2O_7$:Ln^{3+} (Ln = Sm, Eu): time-resolved photoluminescence, EXAFS, and DFT measurements, *Inorg. Chem.*, 2017, **56**(1), 167–178.
32 Y. Liu, G. Liu, X. Dong, J. Wang and W. Yu, Luminescence, energy-transfer and tunable color properties of single-component Tb^{3+} and/or Sm^{3+} doped $NaGd(WO_4)_2$ phosphors with UV excitation for use as WLEDs, *RSC Adv.*, 2014, **4**(102), 58708–58716.
33 L. Wang, H. M. Noh, B. K. Moon, S. H. Park, K. H. Kim, J. Shi and J. H. Jeong, Dual-mode luminescence with broad near UV and blue excitation band from Sr_2CaMoO_6:Sm^{3+} phosphor for white LEDs, *J. Phys. Chem. C*, 2015, **119**(27), 15517–15525.
34 R.-R. Wang, G.-H. Li and G.-M. Cai, Thermal-stability synergy improvement of Sm^{3+} and Eu^{3+} in $Ca_{3.6}In_{3.6}(PO_4)_6$: the effect of local symmetry, *J. Mater. Chem. C*, 2023, **11**(10), 3616–3625.
35 L. Xia, Z. Mao, X. Wang, J. Zhu, J. Xie, Z. Wang and W. Hu, Superlattice-stabilized structure and charge transfer assisted photoluminescence enhancement in a samarium-doped high entropy perovskite oxide, *J. Mater. Chem. C*, 2023, **11**(29), 9899–9907.
36 H. Xiong, X. Gao, F. Yuan, Q. Wu, W. Zhang and Y. Huang, Photoluminescence enhancement of orange-emitting $Ca_5(PO_4)_2SiO_4$:Sm^{3+} phosphor through charge compensation of A^+(Li^+, Na^+ and K^+) ions for white light-emitting diodes, *Dalton Trans.*, 2022, **51**(22), 8874–8884.
37 C. Xu, C. Li, D. Deng, J. Lu, H. Yu, L. Wang, X. Jing, S. Xu and C. Shao, A dual-mode optical thermometer with high sensitivity based on $BaAl_{12}O_{19}$:Sm^{2+}/$SrAl_{12}O19$:Sm^{3+} solid solution phosphors, *Inorg. Chem.*, 2022, **61**(20), 7989–7999.
38 J. Xu, Z. Ju, X. Gao, Y. An, X. Tang and W. Liu, $Na_2CaSn_2Ge_3O_{12}$: a novel host lattice for Sm^{3+}-doped long-persistent phosphorescence materials emitting reddish orange light, *Inorg. Chem.*, 2013, **52**(24), 13875–13881.
39 J. Grigorjevaite, E. Ezerskyte, J. Páterek, S. Saitzek, A. Zabiliūtė-Karaliūnė, P. Vitta, D. Enseling, T. Jüstel and A. Katelnikovas, Luminescence and luminescence quenching of K2Bi(PO4)-(MoO4):Sm3+ phosphors for horticultural and general lighting applications, *Mater. Adv.*, 2020, **1**(5), 1427–1438.
40 J. Li, J. Liu, Q. Ni, Q. Zhu, Z. Zeng, J. Huo, C. Long and Q. Wang, Key role effect of samarium in realizing zero thermal quenching and achieving a moisture-resistant reddish-orange emission in $Ba_3LaNb_3O_{12}$:Sm3+, *Inorg. Chem.*, 2022, **61**(44), 17883–17892.
41 B. Zhao, L. Yuan, S. Hu, X. Zhang, X. Zhou, J. Tang and J. Yang, Controllable synthesis of $Sc_2Mo_3O_{12}$ microcrystals with exposed {001} facets and their remarkable tunable luminescence properties by doping lanthanides, *CrystEngComm*, 2016, **18**(41), 8044–8058.
42 B. Ravel and M. Newville, ATHENA, ARTEMIS, HEPHAESTUS: data analysis for X-ray absorption spectroscopy using IFEFFIT, *J. Synchrotron Radiat.*, 2005, **12**(4), 537–541.
43 R. D. Shannon, Revised effective ionic radii and systematic studies of interatomic distances in halides and chalcogenides, *Acta Crystallogr., Sect. A: Cryst. Phys., Diffr., Theor. Gen. Crystallogr.*, 1976, **32**(5), 751–767.
44 S. K. Gupta, B. Modak, J. Prakash, N. Rawat, P. Modak and K. Sudarshan, Modulating the optical and electrical properties of oxygen vacancy-enriched $La_2Ce_2O_7$:Sm^{3+} pyrochlore: role of dopant local structure and concentration, *New J. Chem.*, 2022, **46**(9), 4353–4362.
45 A. Balhara, S. K. Gupta, B. Modak, H. V. Annadata, G. D. Patra, D. Tyagi and B. Ghosh, Local Structure and Speciation-Driven UO_2^{2+} → Sm^{3+} Energy Transfer for Enhanced Luminescence in $Li_2B_4O_7$, *Inorg. Chem.*, 2023, **62**(49), 20258–20270.
46 K. Singh, M. Rajendran, R. Devi and S. Vaidyanathan, Narrow-band red-emitting phosphors with high color purity, trifling thermal and concentration quenching for hybrid white LEDs and $Li_3Y_3BaSr(MoO_4)_8$:Sm^{3+},Eu^{3+}-based deep-red LEDs for plant growth applications, *Inorg. Chem.*, 2022, **61**(6), 2768–2782.
47 L. Pu, P. Li, J. Zhao, Y. Wang, D. Guo, L. Li, Z. Wang and H. Suo, Eu^{3+}-Activated Single-Band Ratiometric Nanothermometry by Lattice Negative Thermal Expansion, *Laser Photonics Rev.*, 2023, **17**(8), 2200884.
48 M. Maczka, K. Hermanowicz and J. Hanuza, Phase transition and vibrational properties of $A_2(BO_4)_3$ compounds (A = Sc, In; B = Mo, W), *J. Mol. Struct.*, 2005, **744–747**, 283–288.
49 W. Song, B. Yuan, X. Liu, Z. Li, J. Wang and E. Liang, Tuning the monoclinic-to-orthorhombic phase transition temperature of $Fe_2Mo_3O_{12}$ by substitutional co-incorporation of Zr^{4+} and Mg^{2+}, *J. Mater. Res.*, 2014, **29**(7), 849–855.

